Applied Mathematical Sciences, Vol. 3, 2009, no. 14, 677 - 692

On the Numerical Simulation of Induced Anisotropy in Polar Ice

G. Gödert and F. T. Suttmeier[1]

Abstract

The aim of this work is to present a phenomenological constitutive flow model for polar ice derived from so-called mesoscopic considerations and its consistent implementation into an appropriate finite element scheme. A systematic investigation of the development of texture in isothermal polar ice is presented. From the viewpoint of numerics the flow of ice is considered as a stationary free surface Stokes flow fully coupled with the development of its texture. Boundary conditions at the free surface are accomodated in the course of the computation to the actual flow situation. It turned out that the choice of the velocity boundary conditions at the bottom (bed-rock) is the crucial point in modelling induced anisotropy of free surface flow.

Mathematics Subject Classification: 65N30 (primary) 86A40 (secondary)

Keywords: glaciology, finite element method

1 Introduction

In the context of climate simulations the flow of polar ice masses represents an essential part. In so far there emerges a need for appropriate climate boundary conditions, Greve e.a. [10], Huybrechts [12], Fabre e.a. [4]. Furthermore there is a need of an appropriate description of thermo-mechanical material behaviour. For instance simulations considering future climate need reliable constitutive relations to generate reliable predictions about the global hydrobalance. In addition problems emerged from cold region structural engineering, e.g. Calov e.a. [2], are often become more reliable through such flow simulations. On the other hand, because it may record the past history of ice and climatic changes and because it is sensible to ice sheets deformation history, the microstructure of polar ice is worth studying. The extreme anisotropy of the ice single crystal leads to heterogeneous intra-granular deformation modes within the polycrystal and hence to the development of a certain fabric. The

[1]Correspondence to: suttmeier@mathematik.uni-siegen.de

expectation is, that the climate becomes to some extent reconstructable from analyzing ice-core textures, e.g., Thorsteinsson [17], in combination with the numerical solution of the ice-sheet flow problem. Therefore the following considerations are based on two geometric scales. Recalling that the anisotropy of ice crystallites is given by their c-axes the fine-scale is given by the crystallites orientation defined on the sphere S^2, whereas the large-scale is to be identified with the space of daily experience say $\mathbb{R}^d$. Following Gödert [9] the fine-scale-structure is actually considered via the second-order structure tensor $\mathbf{A}$ denoting mean orientation densities and yielding an anisotropic material behaviour. Equations appropriate for the solid creep of isotropic polar ice are those of a slow, gravity-driven, viscous, incompressible flow, e.g., Fowler [5]. Consequentely, this set of equations has to be extended by an evolution equation for the anisotropic state variable $\mathbf{A}$, see below. Therefore, as a fundamental problem, we consider on a time intervall $(0, t_M)$ the following model, which in compact formulation reads

$$\operatorname{div} \mathbf{v} = 0 \tag{1.1}$$

$$\operatorname{div} \mathbf{T} + \nabla p = \begin{pmatrix} 0 \\ -g \end{pmatrix} \tag{1.2}$$

$$\mathbf{D} = \mathcal{C}_{\mathbf{a}}[\mathbf{T}] \tag{1.3}$$

$$\dot{\mathbf{A}} = \mathcal{E}[\mathbf{v}, \mathbf{A}] \tag{1.4}$$

and holds on a bounded domain Ω in $\mathbb{R}^2$. The right-hand-side $\mathbf{f} = (0, -g)^T$ is defined by the gravity force g. $\mathcal{C}_{\mathbf{a}}$ describes the constitutive relation between the deviatoric stress $\mathbf{T}$ and the strain rate $\mathbf{D} = (\nabla \mathbf{v} + (\nabla \mathbf{v})^T)/2$ and may be identified with the 4-th order fluidity tensor. Due to incompressibility $\mathcal{C}_{\mathbf{a}}$ is bijective only with respect to the deviatoric tensors.
The velocity field is denoted by $\mathbf{v} = (v_1, v_2)^T$ and the related pressure by p. Furthermore $\mathcal{C}_{\mathbf{a}}$ depends on the orientation $\mathbf{A} = (a_{11}, a_{22}, a_{33}, a_{12})^T$ of the crystallites the ice consists of. The corresponding evolution of $\mathbf{A}$ is determined by $\mathcal{E}[\mathbf{v}, \mathbf{A}]$.
Following Gödert [9], $\mathcal{E}$ is given by

$$\begin{aligned}\mathcal{E}[\mathbf{v}, \mathbf{A}] = ((\alpha_1 - 1) I_{\mathrm{dev}} - 2\alpha_1 \mathcal{P}_{\mathbf{a}}) \mathbf{D}(\mathbf{v}) \\ + \lambda_0 (Id - (d+1)\mathbf{A}) + \mathbf{W}\mathbf{A} - \mathbf{A}\mathbf{W} - (\mathbf{v} \cdot \nabla)\mathbf{A},\end{aligned}$$

where $\mathbf{W} = (\nabla \mathbf{v} - (\nabla \mathbf{v})^T)/2$, I_{dev} denotes the identity on Σ.

$$\alpha_1 := \alpha \frac{d}{d-1} (I_{\mathbf{A}^2} - \frac{1}{d}) \tag{1.5}$$

denotes a measure of alignment, $\alpha_1 \to 0$ for randomly distributed c-axes orientations, whereas $\alpha_1 \to \alpha$ if all c-axes are parallel. Furthermore $\alpha = 1.2$ is

determined via field data (c.f. Gödert [8]) and $I_{\mathbf{A}^2}$ denotes the inner product, $I_{\mathbf{A}^2} := (Id, \mathbf{A}^2)$. The macro-space dimension is given by d, λ_0 controls the diffusion due to recrystallisation, e.g. Gödert [9].
The operator $((\alpha_1 - 1)I_{\text{dev}} - 2\alpha_1\mathcal{P}_{\mathbf{a}})$ is realised as a 4×4-matrix, applied to the vector

$$\mathbf{D}(\mathbf{v}) = (\partial_x v_1, \partial_y v_2, 0, (\partial_y v_1 + \partial_x v_2)/\sqrt{2})^T .$$

$\mathcal{P}_{\mathbf{a}}$ is symmetric and in this note given by

$$\mathcal{P}_{\mathbf{a}} = \begin{pmatrix} 2a_{11}(1-a_{11}) & -2a_{11}a_{22} & -2a_{11}(1-a_{11}-a_{22}) & \sqrt{2}(a_{12}-2a_{11}a_{12}) \\ & 2a_{22}(1-a_{22}) & -2a_{22}(1-a_{11}-a_{22}) & \sqrt{2}(a_{12}-2a_{22}a_{12}) \\ & & -(\mathcal{P}_{\mathbf{a}})_{13} - (\mathcal{P}_{\mathbf{a}})_{23} & -2\sqrt{2}a_{12}(1-a_{11}-a_{22}) \\ & & & (a_{11}+a_{22}-4a_{12}a_{12}) \end{pmatrix} .$$

The material behaviour is characterised by

$$\mathcal{C}_{\mathbf{a}} = \mu \left[\frac{\beta}{2} I_{\text{dev}} + (1-\beta)\mathcal{P}_{\mathbf{a}} \right] \tag{1.6}$$

where in accordance to Gagliardini and Meyssonnier [6] $\beta = 0.25$ can be interpreted as the ratio of the prismatic and the basal fluidity. Furthermore μ is given by

$$\mu = \mu_0 \frac{5}{3\beta + 2} ,$$

with a constant $\mu_0 > 0$. In test calculations below we simply choose $\mu_0 = 1$.
For the term $\mathbf{WA} - \mathbf{AW}$, one obtains

$$\mathbf{WA} - \mathbf{AW} = \frac{(\partial_y v_1 - \partial_x v_2)}{2} \begin{pmatrix} 2a_{12} & -2a_{12} & 0 & a_{22} - a_{11} \end{pmatrix}^T .$$

Assuming initially randomly distributed c-axes the above equations give the local evolution of the fluidities as well as of the (in-plane) eigensystem of the structure tensor due to simple shear deformation as it is depicted in Fig.(1_a) for $\mu = const.$
Fig.(1_b) gives the evolution of eigensystem in the plane deformation takes place. Starting from an isotropic configuration, inner circle, the maximum direction evolves close to a completely aligned state given by the outer circle.
Note, that in the stationary state $\frac{\sigma_{ii_\infty}}{\sigma_{12_\infty}} \approx 3 \in [8/3, 8]$, which is in agreement with the results given in Budd and Jacka [1], whereas the absolute shear-flow acceleration expected from experimental measurement is not achieved, Fig.(1_c) However, the enhancement of the shear flow can be done by an enhanced fluidity controlled by the orientational state of the polycrystal (enhancement factor).

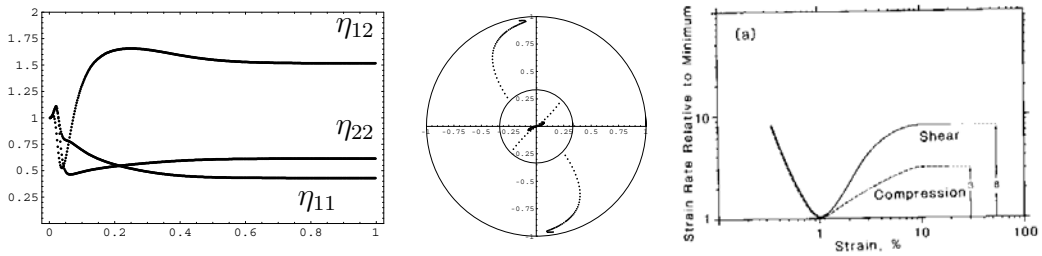

Figure 1: Homogeneous simple shear flow: a) Evolution of the effective shear and compressive fluidities η_{11}, η_{22}, η_{12} due to simple shear, $\lambda_0 = 0$. b) Evolution of the maximum eigen-direction. c) Schematic evolution of the effective fluidities under shear and compressive loading, respectively, from Budd and Jacka (1989).

The basis for applying the Finite Element (FE) method to the system (1.1)–(1.4) is the formulation in an adequate variational setting. To this end, we eliminate the stress $\mathbf{T}$ and introduce

$$U = \begin{pmatrix} \mathbf{v} \\ p \\ \mathbf{A} \end{pmatrix} \ , \Phi = \begin{pmatrix} \mathbf{w} \\ q \\ \mathbf{G} \end{pmatrix} . \tag{1.7}$$

With these definitions, we consider the problem of finding $U \in \mathbf{V} := V \times W \times L$ with
$\mathbf{V} \subset (H^1)^2 \times L^2 \times (H^1)^4$, fulfilling

$$\mathcal{B}(U;\Phi) = 0 \qquad \forall\ \Phi \in \mathbf{V}\,, \tag{1.8}$$

with

$$\mathcal{B}(U;\Phi) := (\mathcal{C}_{\mathbf{a}}^{-1}[\mathbf{D}(\mathbf{v})], \mathbf{D}(\mathbf{w})) + (\operatorname{div}\mathbf{w}, p) + (\operatorname{div}\mathbf{v}, q) \\ - (\mathbf{f}, \mathbf{w}) - (\dot{\mathbf{A}}, \mathbf{G}) + (\mathcal{E}[\mathbf{v}, \mathbf{A}], \mathbf{G})\,.$$

Here and in what follows, $(.,.)$ represents the L^2 inner product of a bounded domain Ω in $\mathbb{R}^2$ and $\|.\|$ the corresponding norm. Furthermore $H^m = H^m(\Omega)$ denotes the standard Sobolev space of L^2-functions with derivatives in $L^2(\Omega)$ up to the order m, and $H_0^1 \subset H^1$ is the subspace of H^1-functions vanishing on $\Gamma := \partial\Omega$.
Testing by $\Phi = (\mathbf{w}, q, 0)^T$ and $\Phi = (0, 0, \mathbf{G})^T$ yields the weak formulation of the system (1.1)–(1.4)

$$(\mathcal{C}_{\mathbf{a}}^{-1}[\mathbf{D}(\mathbf{v})], \mathbf{D}(\mathbf{w})) + (\operatorname{div}\mathbf{w}, p) + (\operatorname{div}\mathbf{v}, q) = (\mathbf{f}, \mathbf{w})\ \forall (\mathbf{w}, q) \in V \times W \tag{1.9}$$

$$-(\dot{\mathbf{A}}, \mathbf{G}) + (\mathcal{E}[\mathbf{v}, \mathbf{A}], \mathbf{G}) = 0 \qquad \forall \mathbf{G} \in L\,. \tag{1.10}$$

In other words, we treat a coupled system given by the evolution problem (1.10) and the Stokes-like flow (1.9). For abbreviation, we define

$$\mathcal{S}(A;\{\mathbf{v},p\},\{\mathbf{w},q\}) := (\mathcal{C}_{\mathbf{a}}^{-1}[\mathbf{D}(\mathbf{v})],\mathbf{D}(\mathbf{w})) + (\operatorname{div}\mathbf{w},p) + (\operatorname{div}\mathbf{v},q)\,. \quad (1.11)$$

2 Discretisation

The full discretisation for the system (1.8) is derived in two steps. First, we perform a discretisation with respect to the time variable, yielding a sequence of problems continuous with respect to the space variable. In the second step, these problems are approximated by the finite element method.

2.1 Semi-discretisation

For discretization, the time interval $[0,t_M]$ is decomposed like $0 = t_0 < t_1 < \ldots < t_M$ into subintervals $I_m := (t_{m-1},t_m]$ of length $k_m := t_m - t_{m-1}$. Integrating in (1.8) over I_m yields

$$\int_{I_m} \Big[\mathcal{S}(A;\{\mathbf{v},p\},\{\mathbf{w},q\}) - (\mathbf{f},\mathbf{w})\Big]\,dt \\ - (\mathbf{A}^m,\mathbf{G}) + (\mathbf{A}^{m-1},\mathbf{G}) + \int_{I_m} (\mathcal{E}[\mathbf{v},\mathbf{A}],\mathbf{G})\,dt = 0\,, \quad (2.12)$$

for all $\{\mathbf{w},q,\mathbf{G}\} \in \mathbf{V}$. The integrals are approximated by quadrature formulas of the type

$$\int_{I_m} w(t)\,dt = k_m\{\alpha w^m + (1-\alpha)w^{m-1}\}\,, \quad (2.13)$$

with some $\alpha \in (0,1]$. The choice of $\alpha = 1$ corresponds to the backward Euler scheme, while for $\alpha = \frac{1}{2}$, we obtain the Crank-Nicolson scheme. Here, we only consider the simple Euler scheme which reads

$$B(U^m;\Phi) := k_m\mathcal{S}(A^m;\{\mathbf{v}^m,p^m\},\{\mathbf{w},q\}) - (\bar{\mathbf{f}}^m,\mathbf{w}) \\ - (\mathbf{A}^m,\mathbf{G}) + (\mathbf{A}^{m-1},\mathbf{G}) + k_m(\mathcal{E}[\mathbf{v}^{\mathbf{m}},\mathbf{A}^{\mathbf{m}}],\mathbf{G}) = 0\,, \quad (2.14)$$

with the averaged forcing terms $\bar{\mathbf{f}}^m = \int_{I_m} \mathbf{f}\,dt$. In what follows the superscript m is omitted.

2.2 Solution process

In this section, we describe the algorithm (see e.g. Geiger and Kanzow [7]) we employ to solve the problems arising in (2.14) having the general structure

$$B(U;\Phi) = 0\,. \quad (2.15)$$

1. Calculate correction D^j by a linear problem
$$L_B(D^j, \Phi) = B(U^j; \Phi)\,. \tag{2.16}$$
2. Perform a damped update
$$U^{j+1} = U^j - \alpha^j D^j\,, \tag{2.17}$$
where α^j is choosen s.t.
$$B(U^{j+1}; \Phi) \leq B(U^j; \Phi) + \alpha^j \delta D^j B(U^j; \Phi) \tag{2.18}$$
with a constant $\delta \geq 0$.
3. Set $j = j + 1$ and goto 1.

Example: The Newton scheme is defined by the choice
$$L_B(D^j, \Phi) = B'(U^j; D^j, \Phi)\,, \tag{2.19}$$
where $B'(U^j; \cdot, \cdot)$ is the derivative of $B(\cdot; \cdot)$ in U^j.

2.3 Simplified Newton-scheme

In what follows, we sketch the application of the strategy described above for solving the time discrete problems (2.14).
In step j of the solution process above, the linear operator L_B in (2.16) to get a full Newton-scheme is written
$$L_B = \begin{pmatrix} L_{11} & L_{12} & L_{13} \\ L_{21} & L_{22} & L_{23} \\ L_{31} & L_{32} & L_{33} \end{pmatrix}\,, \tag{2.20}$$
where with $\{X\} = \{\mathbf{v}, p, \mathbf{A}\} = \{\mathbf{v}^j, p^j, \mathbf{A}^j\}$ we define
$$\begin{array}{lll} L_{11} = \partial_{\mathbf{v}} B(\{X\}; \{\mathbf{w}, 0, 0\})\,, & L_{12} = \partial_p B(\{X\}; \{\mathbf{w}, 0, 0\})\,, & L_{13} = \partial_{\mathbf{A}} B(\{X\}; \{\mathbf{w}, 0, 0\})\,, \\ L_{21} = \partial_{\mathbf{v}} B(\{X\}; \{0, q, 0\})\,, & L_{22} = \partial_p B(\{X\}; \{0, q, 0\})\,, & L_{23} = \partial_{\mathbf{A}} B(\{X\}; \{0, q, 0\})\,, \\ L_{31} = \partial_{\mathbf{v}} B(\{X\}; \{0, 0, \mathbf{G}\})\,, & L_{32} = \partial_p B(\{X\}; \{0, 0, \mathbf{G}\})\,, & L_{33} = \partial_{\mathbf{A}} B(\{X\}; \{0, 0, \mathbf{G}\})\,. \end{array}$$

As a first simplification in order to get a block-diagonal system which can easily be solved, we choose
$$L_B = \begin{pmatrix} L_{11} & L_{12} & 0 \\ L_{21} & L_{22} & 0 \\ 0 & 0 & L_{33} \end{pmatrix}\,. \tag{2.21}$$
Additionally, we approximate
$$\begin{array}{ll} L_{11} \approx \partial_{\mathbf{v}} B(\{\mathbf{v}, p, \mathbf{A}^{j-1}\}; \{\mathbf{w}, 0, 0\})\,, & L_{22} \approx \partial_p B(\{\mathbf{v}, p, \mathbf{A}^{j-1}\}; \{0, q, 0\})\,, \\ L_{12} \approx \partial_p B(\{\mathbf{v}, p, \mathbf{A}^{j-1}\}; \{\mathbf{w}, 0, 0\})\,, & L_{33} \approx \partial_{\mathbf{A}} B(\{\mathbf{v}^{j-1}, p^{j-1}, \mathbf{A}\}; \{0, 0, \mathbf{G}\})\,. \end{array}$$

2.4 Spatial discretisation

In order to obtain approximate solutions of the time discrete problems (2.14) we will apply the finite element method on decompositions $\mathbb{T}_h = \{T_i \mid 1 \leq i \leq N_h\}$ of Ω consisting of quadrilateral elements T, satisfying the usual condition of shape regularity. The width of the mesh $\mathbb{T}_h$ is characterised in terms of a piecewise constant mesh size function $h = h(x) > 0$, where $h_T := h_{|T} = \mathrm{diam}(T)$. With these notations the discrete solutions U_h of (2.14) are defined by

$$B(U_h;\Phi) := \mathcal{S}(A_h;\{\mathbf{v}_h,p_h\},\{\mathbf{w},q\}) - (\bar{\mathbf{f}},\mathbf{w}) - (\mathbf{A}_h,\mathbf{G}) + (\mathbf{A}_h^{m-1},\mathbf{G}) + k_m(\mathcal{E}[\mathbf{v},\mathbf{A}],\mathbf{G}) = 0\,, \quad (2.22)$$

for all $\{\mathbf{w},\mathbf{q}\} \in V_h \times W_h \times L_h$, where V_h and L_h are constructed by the standard bilinear and W_h by piecewise constant shape functions.
For ease of mesh refinement and coarsening, hanging nodes are allowed in our implementation.

3 Numerical results

The numerical results presented throughout this work are obtained by FE-implementations based on the DEAL-library [3].

3.1 Boundary conditions

Ice sheets are *cold*, i.e. below their melting point, except at parts of their base, where the temperature may reach the melting point. For instance, this can be concluded from radio-echo sounding of sub-Antarctic lakes (c.f. Oswald and Robin [14]). The usual fluid no-slip boundary conditions only apply when basal ice is cold, but at the melting temperature, ice can slide over its base (see Paterson [15]). In Fowler [5] it is mentioned, that several models are based on the assumption of non-zero sliding velocity, and in some cases this is even required in order to obtain a solution (see Morland and Johnson [13] and Hutter e.a. [11]). On the other hand, basal topographie in Antarctica is so rough, that for the sliding law we should expect $\mathbf{v} \approx 0$ (c.f. Paterson [15], Richardson [16]).
Following these remarks we consider in test configurations sketched in Figure 2

1. no-slip boundary conditions, i.e. $v_1 = v_2 = 0$ on $\Gamma_x\,, \quad v_1 = 0$ on $\Gamma_y\,,$
2. slip boundary conditions, i.e. $v_2 = 0$ on $\Gamma_x\,, \quad v_1 = 0$ on $\Gamma_y\,,$
3. combined boundary conditions, i.e. on $(0, t_m = 5)$ we apply the slip condition, on $(t_m, t_M = 20)$ we apply the no-slip condition,

for the components of the velocity field $\mathbf{v} = (v_1, v_2)^T$.

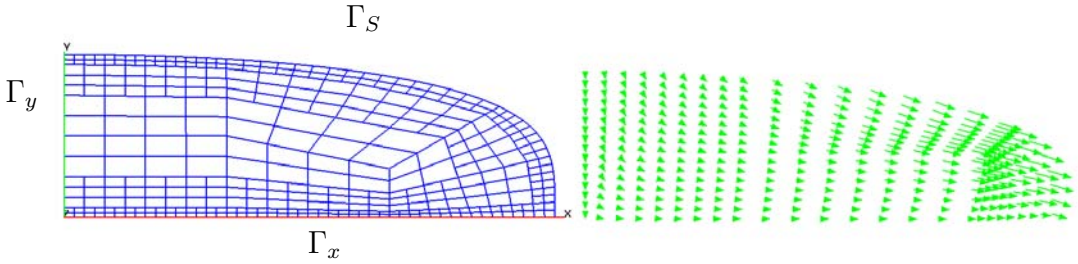

Figure 2: Sketch of computational domains for the test examples including structure of the FE-meshes for the benchmark problem.

Furthermore, we have free boundary conditions for the components of $\mathbf{A}$ on Γ_x and Γ_y and for $\mathbf{v}$ on $\Gamma_S := \partial\Omega \setminus (\Gamma_x \cup \Gamma_y)$.
Now, we first calculate the deformation under the assumption of isotropic material behaviour.A plot of the velocity field is depicted in Figure 2. We observe that Γ_S is devided into two parts, the inflow and outflow boundary, defined by

$$\Gamma_- = \{x \in \Gamma_S \mid v \cdot n < 0\}\,, \tag{3.23}$$
$$\Gamma_+ = \{x \in \Gamma_S \mid v \cdot n \geq 0\}\,, \tag{3.24}$$

where n denotes the outward unit normal of Γ_S. Consequently, we can prescribe inflow boundary data for the components of $\mathbf{A}$ on Γ_-. On Γ_+ $\mathbf{A}$ is left free.

3.2 Benchmark problem

Here, we consider our model on a bounded domain Ω described by

$$1 - \tfrac{2}{3}\varepsilon x^2 - y^4 = 0 \qquad \varepsilon = 1.83 \cdot 10^{-2}\,.$$

The structure of the FE-meshes is shown in Figure 2. Especially, we focus on the evaluation of the velocity field along axis parallel to the $y-$axis.
In order to check our discretisation, we compare the computed solution of v_1 along the vertical line $x = 1$ for the isotropic case to Vialov's profile (c.f. Vialov [18]), an analytical description for such a situation. The result is depicted in Figure 3, demonstrating good agreement between computed and the exact solution, denoted by u and $f(x)$ respectively.

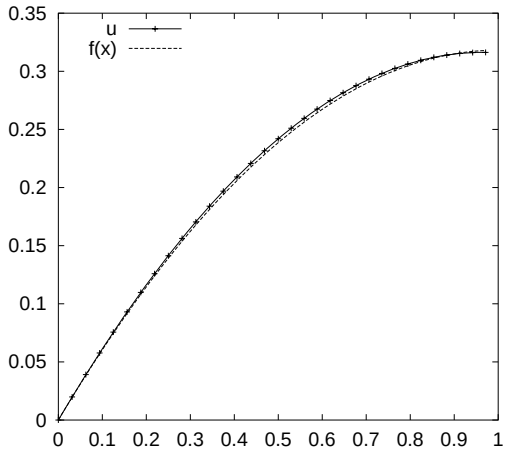

Figure 3: Evaluation of u along vertical line.

Now, evaluating the global L^2-norm

$$\Delta(A_h^m) := \left(\int_\Omega (k_m^{-1}(A_h^m - A_h^{m-1}))^2 \, dx \right)^{1/2}$$

for each time step t_m, the time dependent process is observed to converge to a stationary solution, i.e., $\Delta(A_h^m)$ tends to zero, which is illustrated in Figure 4. In what follows, we show the results for the times $t = 0, 5, 10, 15, 20$. We investigate the evolution of the distribution of anisotropic behaviour of the ice in dependance of the boundary conditions.

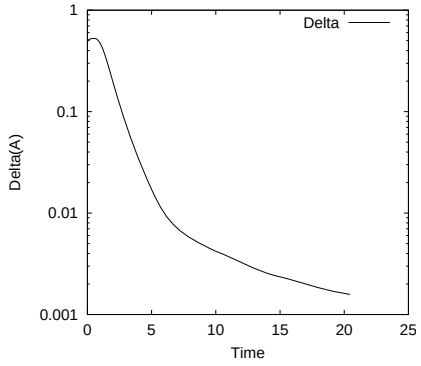

Figure 4: Evaluating $\Delta(A_h^m)$ indicates the time dependent process to converge to a stationary solution.

Anisotropy is measured here by evaluating the maximum eigenvalue λ and its

associated direction $\mathbf{a} = (-\sin\varphi_\lambda, \cos\varphi_\lambda)$ of

$$\mathbf{A} = \begin{pmatrix} a_{11} & a_{12} & 0 \\ a_{12} & a_{22} & 0 \\ 0 & 0 & a_{33} \end{pmatrix},$$

and the orientation of the corresponding eigenvector, which is given by

$$\varphi_\lambda = \arctan \frac{a_{12}}{z - \sqrt{z^2 + a_{12}^2}} \quad \text{with } z = \frac{1}{2}(a_{11} - a_{22})$$

$$\text{and} \quad \lambda = \frac{1}{2}(a_{11} + a_{22}) + \sqrt{(z^2 + a_{12}^2)}$$

Here $\lambda = 1/3$ indicates isotropic behaviour.

3.3 Time step control

The computations are performed using about 23365 degrees of freedom. The time step is choosen adaptively via

$$k_m = 0.9 k_{m-1} \sqrt{\delta / \|U_1 - U_2\|}\,.$$

with $\delta = 0.001$. Here U_1 and U_2 denote the solution at time step $m-1$ obtained by employing Euler and Crank-Nicolson scheme respectively. The typical developement of the local step size is depicted in Figure 5 showing k_m to increase in the stationary limit. The considerations are restricted to isothermal flow.

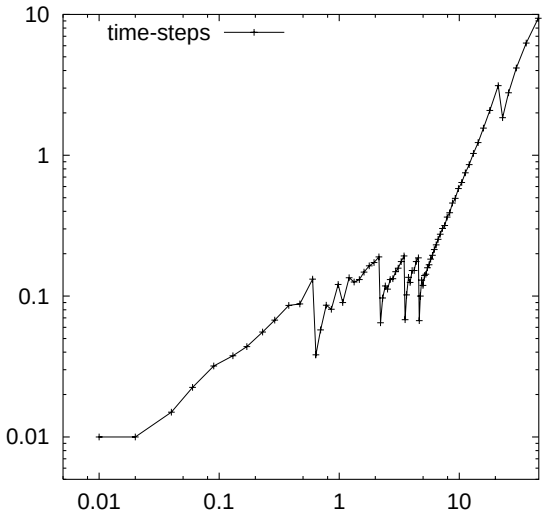

Figure 5: Typical developement of the local step size during the simulation, showing k_m to increase in the stationary limit.

3.4 Results

First in Figure 6, we show the evolution of a_{22}, which is somehow related to the degree of anisotropy, within the timedependent process in the case of no-slip boundary conditions. We observe the developement of a (nearly) fully aligned region (red domain).

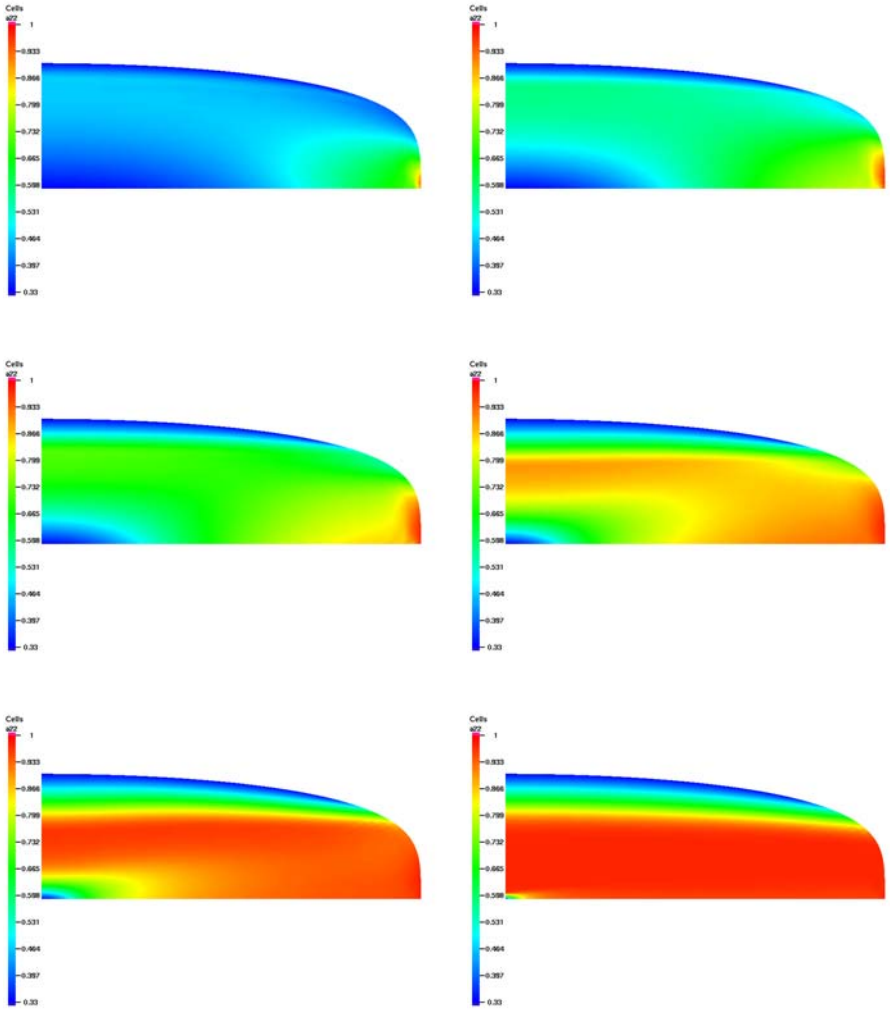

Figure 6: Evolution of a_{22} within the timedependent process.

Figures 7 and 8 shows the evolution of the maximum eigenvalue as well as the direction of the associated eigenvector of the second order structure tensor, $\mathbf{A}$, along a vertical cross section at $x = 1$. It turns out that the evolution of the structure tensor does strongly depend on the boundary conditions at the bottom. In order to investigate this systematically the results for slip (left),

no-slip (center)and combined boundary conditions (right) are given in each row. All other parameters are kept the same.

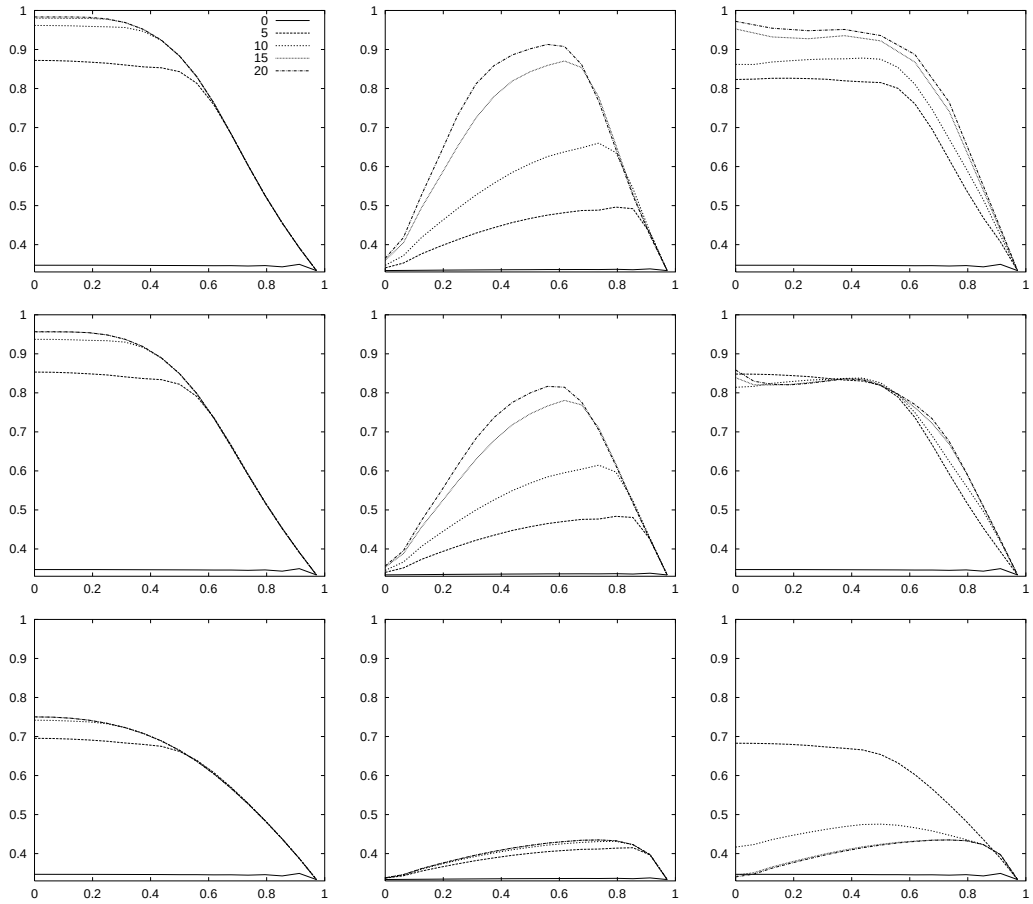

Figure 7: Evolution of the maximum eigenvalue along vertical line for $t = 0, 5, 10, 15, 20$. Results for slip (left), no-slip (center), combined (right) for $\lambda_0 = 0.0$ (top), $\lambda_0 = 0.1$ (middle) and $\lambda_0 = 1.0$ (bottom)

Yet, the application of combined conditions can be motivated by physical arguments: Because an ice shield evolves continuously over centuries it seems to be inadequate considering the stationary configuration with
isotropic initial values for the internal structure. A more appropriate initial configuration is obtained if we consider slip boundary conditions at the bottom for $t \in [0, 5]$ yielding an anisotropic initial configuration similar to that found in polar ice. In accordance to related work (*cf.* [6]), subsequently, i.e. for $t \in [5, 20]$, the nodes at the bottom are hold fixed (no-slip). Furthermore we examined the influence of diffusion on the solution. The results for $\lambda_0 = 0.0$, $\lambda_0 = 0.1$ and $\lambda_0 = 1.0$ are depicted in the first, second and third row, respectively.

Analysing the evolution of the eigenvalue λ along the vertical line at $x = 1$ from the surface down to the base, we observe for the no-slip condition (Figure 7, center column) an increase from 1/3 (isotropic) at the top to $\lambda \approx 1$ close to the bottom (anisotropic). Eventually, approaching the base, λ decreases back to 1/3 (isotropic).

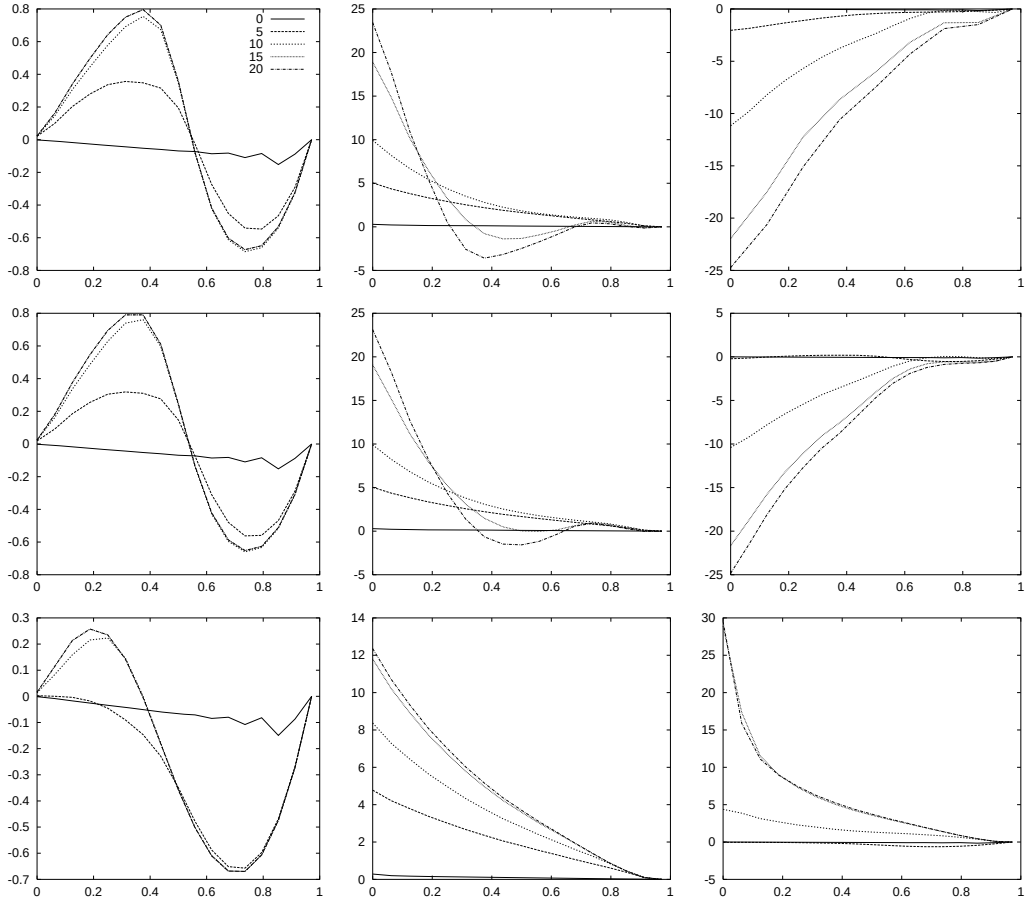

Figure 8: Evolution of the orientation along vertical line for $t = 0, 5, 10, 15, 20$. Results for slip (left), no-slip (center), combined (right) for $\lambda_0 = 0.0$ (top), $\lambda_0 = 0.1$ (middle) and $\lambda_0 = 1.0$ (bottom)

In contrast, evaluating λ for the slip condition (Figure 7, first column), we observe a monoton increase of anisotropy from surface down to the base. Additionally, these pictures illustrate, that the maximum eigenvalue, λ, is controlled by the diffusion coefficient λ_0.
In Figure 8, we investigate the evolution of the orientation φ_λ. The case of slip conditions implies $\varphi_\lambda = 0$ at top and bottom (first column). The deviation of the associated eigenvector from the vertical axis is bounded by $[-1°, 1°]$. In contrast we observe for moderate diffusion an oscillation with increasing

amplitude along the depth if no-slip conditions are applied. Depending on λ_0 distortions of the orientation are within $[-5°, 25°]$. A monotonic increase of φ_λ is obtained for strong diffusion, i.e. $\lambda_0 = 1$.
In comparison to no-slip boundary conditions the distortion for combined conditions and moderate diffusion does evolve in the opposite direction. However, the no-slip eigenvalues in the vicinity to the base generate a more or less isotropic internal structure.
Figure 9 compares the normalised, stationary, horizontal velocity field along the cross section at $x = 1$ for no-slip conditions and different values of $\lambda_0 = 0.0, 0.1, 1.0$ with Vialov's solution: The curvature of the profile increases if λ_0 decreases, that is the velocity field can be controlled by the diffusion. This suggests an acceleration of the glacier if anisotropy is taken into account.

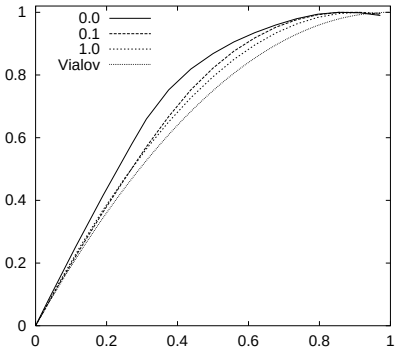

Figure 9: Qualitative comparison of the normalised, stationary, horizontal velocities for $\lambda_0 = 0.0, 0.1, 1.0$ with Vialovs solution

4 Conclusion

A systematic investigation of the development of texture in isothermal polar ice was presented. Based on the statistical concept of orientation distribution functions texture was represented by a second order structure tensor supplemented by an appropriate evolution equation. Amendatory to related work we took also recrystallisation effects into account as far as they may be modelled by diffusion type constitutive equations, where diffusion is simply controlled by the parameter λ_0. A fully coupled numerical procedure considers anisotropy as an additional degree of freedom. Hence, there is a need of appropriate boundary conditions (bc's) not alone for the velocities but also for the components of the structure tensor. Irrespective of the actual boundary conditions and of λ_0 the model ice sheet developed a layered structure with respect to the intensity of the texture. However, as it is known from analytical treatments,

the choice of appropriate velocity boundary conditions at the bottom (bedrock) turned out to be a crucial point in modelling induced anisotropy of free surface flow. This is indicated by the fact, that if no-slip conditions are applied at the bottom (nearly) isotropic behaviour results for the basal ice even if $\lambda_0 = 0$ (no recrystallisation), whereas slip conditions allow for more realistic evolution of anisotropies over the whole glacier. In so far we conclude that slip bc's seem to be the more adequate choice. Beside the simulated texture this judgement was confirmed also from the viewpoint of numerical stability. Although Figure 9 suggests an acceleration of the glacier it should be noticed that due to the evolution of the anisotropy a decreasing horizontal free-surface velocity is observed, irrespective of the underlying basal boundary conditions and irrespective of the intensity of the diffusion represented via λ_0. Here, our results are in contradiction to [6]. However, for us it seems to be a reasonable response of the material under vertical gravitational loading only. Noting further, that the ratio of the fluidities, see Fig. 1, is in agreement with the values given in the literature, e.g., Budd and Jacka [1], this might be interpreted as a vote for an additional isotropic enhancement factor, controlled by the degree of alignment as well as by the temperature.

References

[1] W.F. Budd and T.H. Jacka. A review of ice rheology for ice sheet modelling. *Cold Reg. Sci. Technol.*, 16:107–144, 1989.

[2] R. Calov, A.A. Savvin, R. Greve, I. Hansen, and K. Hutter. Simulation of the antarctic ice sheet with a three-dimensional polythermal ice sheet model. *Annals of Glaciology*, 27:201–206, 1998.

[3] DEAL. differential equations analysis library . `http://www.math.uni-siegen.de/suttmeier/deal/deal.html` , 1995.

[4] A. Fabre, A. Letreguilly, and C. Ritz. Sensitivity of a greenland ice sheet model to ice flow and ablation parameters: Consequences on the evolution through the last climatic cycle. *Climate Dynamics*, 13:11–24, 1997.

[5] A.C. Fowler. Modelling ice sheet dynamics. *Geophys. Astrophys. Fluid Dynamics*, 63:29–65, 1992.

[6] O. Gagliardini and J. Meyssonnier. Plane flow of an ice sheet exhibiting strain-induced anisotropy. In Y. Wang K. Hutter and H. Beer, editors, *Advances in Cold-Region Thermal Engineering and Sciences*, pages 171–182. Springer, 1999.

[7] C. Geiger and C. Kanzow. *Numerische Verfahren zur Lösung unrestringierter Optimierungsaufgaben*. Springer, 1999.

[8] G. Gödert. Meso-macro model for the description of induced anisotropy of natural ice, including grain interaction. In K. Hutter, Y. Wang, and H. Beer, editors, *Advances in Cold-Region Thermal Engineering and Sciences*, pages 183–196, 1999.

[9] G. Gödert. The use of structure tensors to model the evolution of textural anisotropy of polar ice. *Ann. Glaciol.*, 2002. submitted.

[10] R. Greve, M. Weis, and K. Hutter. Palaeoclimatic and present conditions of the greenland ice sheet in the vicinity of summit: An approach by large-scale modelling. *Paleoclimates*, 2:133–161, 1998.

[11] K. Hutter, S. Yakowitz, and F. Szidarovsky. A numerical study of plane ice sheet flow. *J. Glaciol.*, 32:139–160, 1986.

[12] P. Huybrechts. The present evolution of the greenland ice sheet: an assessment by modelling. *Global Planet. Change*, 9:39–51, 1995.

[13] L.W. Morland and I.R. Johnson. Steady motion of ice sheets. *J. Glaciol.*, 28:229–246, 1980.

[14] G.K.A. Oswald and G.de Q. Robin. Lakes beneath the antartic ice sheet. *Nature*, 245:251–254, 1973.

[15] W.S.B. Paterson. *The physics of glaciers*. Pergamon, Oxford, 1981.

[16] S. Richardson. On the no-slip boundary condition. *J. Fluid Mech.*, 59:707–719, 1973.

[17] T. Thorsteinsson. Textures and fabrics in the grip ice core, in relation to climate history and ice deformation. Technical Report 206, Reports on Polar Research, 1996. ISSN 0176-5027.

[18] S.S. Vialov. Regularities of glacial ice shields movements and the the theory of plastic viscous flow. *Physics of the movements of ice, IAHS*, 47:266–275, 1958.

Received: August, 2008